JOURNAL OF MATERIALS RESEARCH AND TECHNOLOGY 2022;18:4918–4929

Available online at www.sciencedirect.com

jmr&t
Journal of Materials Research and Technology

journal homepage: www.elsevier.com/locate/jmrt

Original Article

Up-scalable synthesis of size-controlled NiSe nanoparticles using single step technique

Naif Mohammed Al-Hada [a,b,*], *Rafiziana Md. Kasmani* [b], *Hairoladenan Kasim* [c,**], *Abbas M. Al-Ghaili* [d,***], *Muneer Aziz Saleh* [e], *Hussein Baqiah* [a], *Bandar Ali Al-Asbahi* [f], *Jianlei Yang* [a], *Azlan Muhammad Noorazlan* [g], *Qiang Li* [a], *Jian Liu* [a], *Abdullah A.A. Ahmed* [h], *Shicai Xu* [a]

[a] *Shandong Key Laboratory of Biophysics, Institute of Biophysics, Dezhou University, Dezhou 253023, China*
[b] *School of Chemical and Energy Engineering, Universiti Teknologi Malaysia, Skudai, Johor Bahru 81310, Malaysia*
[c] *College of Computing and Informatics (CCI), Universiti Tenaga Nasional (UNITEN), 43000 Kajang, Selangor, Malaysia*
[d] *Institute of Informatics and Computing in Energy (IICE), Universiti Tenaga Nasional (UNITEN), Kajang 43000, Malaysia*
[e] *Office of Radiation Protection, Environmental Public Health, Washington State Department of Health, WA, USA*
[f] *Department of Physics & Astronomy, College of Science, King Saud University, P.O. Box 2455, Riyadh 11451, Saudi Arabia*
[g] *Physics Department, Faculty of Science and Mathematics, University Pendidikan Sultan Idris, Tanjong Malim 35900, Malaysia*
[h] *Fachbereich Physik, Center for Hybrid Nanostructures (CHyN), Universität Hamburg, 20146 Hamburg, Germany*

ARTICLE INFO

Article history:
Received 28 March 2022
Accepted 28 April 2022
Available online 5 May 2022

Keywords:
NiSe nanoparticles
Energy band gap
Thermal treatment technique
Optical characteristics
Structural characteristics
Magnetic characteristics

ABSTRACT

Pure NiSe nanoparticles were successfully produced using an adapted thermal treatment technique and an alternate nitrogen flow. Throughout a range of calcination temperatures of 500 °C–800 °C, a number of techniques were utilised in order to examine the optical, structural and magnetic characteristics of the attained NiSe nanoparticles. Ultraviolet-visible absorption spectrophotometry was employed to ascertain the optical characteristics. These evidenced a reduction in the NiSe nanoparticle conduction band with elevated calcination temperatures, i.e. from 3.58 eV to 3.37 eV at 500 °C and 800 °C, respectively. This was attributed to a higher degree of attraction between the conduction electrons and the metallic ions with rising particle dimensions, equating to a larger atom population comprising the metal nanoparticles. This means that the findings can be applied to a wide range of energy applications. The lack of impurities within the produced NiSe nanoparticles was verified utilising Fourier-transform infrared spectroscopy and energy dispersive X-ray analysis. At calcination temperatures of ≥ 500 °C, powder X-ray diffraction demonstrated that the specimen, amorphous at room temperature, had undergone

* Corresponding author.
** Corresponding author.
*** Corresponding author.
E-mail addresses: naifalhada@yahoo.com (N.M. Al-Hada), hairol@uniten.edu.my (H. Kasim), abbasghaili@yahoo.com (A.M. Al-Ghaili).
https://doi.org/10.1016/j.jmrt.2022.04.152

conversion into hexagonal crystalline nanostructures. Transmission electron microscopy confirmed the evolution of size NiSe nanoparticles; mean particle dimensions increased from 21 nm to 54 nm at calcination temperatures of 500 °C and 800 °C, respectively. Electron spin resonance spectroscopy, used to identify the magnetic properties, supported the presence of unpaired electrons.

1. Introduction

There has been considerable interest in the synthesis and description of chalcogenides because of their noteworthy characteristics and possible utility in nanotechnology [1–6]. The Pauli paramagnetic NiSe belongs to the class of transition metal chalcogenides. It exhibits inferior metallic behaviour *En* masse with band voids at 2.0 eV and within the 2.8–3.6 eV spectrum, in its polycrystalline and nano formats, respectively [7]. As a result of electronic structure of nickel (3 d^8 $4s^2$) also the minimal electronegativity variation between nickel and selenium, i.e. 1.9 and 2.4, respectively, NiSe has the capacity to engage to create complexes with diverse stoichiometry [8,9].

In addition to NiSe, alternative semiconductors based on nickel and selenide, such as $NiSe_2$, and Ni_3Se_2, exist and have been recorded for a variety of utilities [10,11]. The latter have attractive electronic and magnetic traits, have been postulated as Pt-free catalysts for the electrochemical synthesis of hydrogen, and was employed for a range of purposes in the materials science sectors, where a plethora of research has been conducted over recent years [12–15]. Nickel sulphide (0.4 eV) and nickel oxide (3.6–4.0 eV) have been mentioned as suitable candidates for use in solar cells because of their band gaps [16–18].

A contemporary study has described the single-phase and morphologically governed manufacture of hierarchical X and examined the catalytic properties of NiS nanosized with respect to the drop of PNP-PAP [7]. Driven by the spectrum of above uses of this type of semiconducting substance, the aim of this study was to produce a semiconducting nanoform of the NiSe material [19,20]. This has been formerly achieved utilising a hydrothermal process. The shape and dimensions of nickel selenium was governed via changing the Ni salt antecedents, capping and dropping chemicals, respectively, the temperature and the length of the reaction [7]. In the present article, the emphasis is on the in-depth description of the manufacture of the NiSe nanoparticles.

Overall, NiSe nanomaterials can be manufactured using a variety of methods. Examples include chemical bath deposition techniques [21], e.g. solvothermal [22–24] or in situ on graphene [25], hydrothermal method [26,27], pulse potential electrodeposition method [28], and electrodeposition method [29]. The various methods have their individual benefits and drawbacks. During solution phase production, it is possible to govern the particle size and the necessary shape. However, when using some techniques, it is not possible to control the desired shape, which can often give rise to particle clustering, as seen with Ni_3Se_2; at times, the sample may also be impure [30,31]. Nevertheless, the latter technique can be upscaled to generate significant amounts of nanomaterial in a relative brief time interval without the addition of reagents, e.g. solvents, reducing agents or surfactant. In contrast, numerous reagents are necessary for the thermal technique, which only enables the synthesis of diminutive material amounts over a relatively prolonged timescale. In the current study, NiSe nanoparticles have been synthesised employing thermal treatment techniques. Altering a number of manufacturing variables has enabled the substance's particle dimensions to be regulated. NiSe nanoparticles produced by varying techniques have been determined to be markedly efficacious and stable with respect to reduction reactions [32–35]. Many of these approaches have produced particles of the desired dimension and structure. However, drawbacks were noted, e.g., complex protocols, the difficulties associated with eliminating impurities, and the synthesis of noxious by-products that adversely impact the environment. In order to surmount some of these issues, the novel suggestion of heat treatment is postulated for the production of NiSe nanoparticles.

The aim of this technique was to produce semiconductor nanomaterials encompassing: metal ferrite nanoparticles, i.e. CdSe [36], $ZnFe_2O_4$, $MnFe_2O_4$, ZnSe [37], and $CoFe_2O_4$; metal chromic nanoparticles, e.g. $ZnCr_2O_4$ [38], CdO [39], (Cr2O3) x (NiO) 1-x [40], Cassiterite [41], $(ZnO)_{0.8}$ $(ZrO_2)_{0.2}$ [42], and binary nickel and silver oxides [43].

To create metal nanoparticles, a thermal treatment method that eliminated oxygen and nitrogen flow was used in an aqueous solution containing both the metal precursor and PVP during calcination. This was a straightforward process; the lack of requirement for additional agents to be admixed into the reactant reduced the expense, and also ensured that it was pro-environmental, as no noxious or unnecessary by-products were discarded into the drains.

Ultraviolet-visible (UV-vis) absorption spectrophotometry, Fourier-transform infrared spectroscopy (FTIR), energy dispersive X-ray analysis (EDX), powder X-ray diffraction (XRD), transmission electron microscopy (TEM), and electron spin resonance (ESR) spectroscopy were used to evaluate the properties of the samples produced.

2. Materials and methods

The metal antecedent comprised nickel nitrate and selenium powder reagents. PVP (MW = 29,000) and deionised water were deployed as the capping agent and solvent, respectively. All reagents were procured as analytical grade materials from Sigma-Aldrich (St. Louis, MO, USA); they were utilised without additional modification.

1 g PVP and 50 mL deionised water were combined to make up the PVP solution at ambient temperature. 0.5 mmol nickel nitrate and 0.5 mmol selenium were admixed into the solution, which was agitated for 180 min in order to yield a homogeneous solution without any evident precipitation. The solution has been decanted into a glass Petri plate and warmed in an oven for 24 h at a temperature of 80 °C; this was to allow any water to evaporate and to produce a solid cake; this was subsequently pulverised in a pestle and mortar to create a regular powder.

The powder was calcined in 100 °C increments between the temperatures of 500 °C and 800 °C, initially for 180 min in oxygen flow so as to degrade the organic compounds, and then for 180 min in nitrogen gas flow in order to extract any oxygen from the oxides prior to synthesising uncontaminated NiSe nanoparticles. The two gases were permitted to flow consecutively into the heat treatment chamber at similar flow rates, i.e. 50 mL/min.

A range of methods were utilised to examine the attained NiSe nanoparticles. The optical characteristics of the prepared samples have been investigated using a UV-vis spectrophotometer (Shimadzu model UV-3600, Shimadzu, Tokyo, Japan); this was conducted at ambient temperature through the 200–800 nm spectrum. FTIR spectrometry (Perkin Elmer model 1650, Perkin Elmer, Waltham, MA, USA) was used to document the infrared spectrum, i.e. 280 – 4000 cm^{-1}, in order to survey the capping agent extraction following calcination. The specimen's elemental constituents were determined by EDX (model Jeol Jsm 7600, Jeol, Tokyo, Japan) following calcination at 600 °C. These results were combined with those from FTIR in order to depict the generation of pure crystalline NiSe nanoparticles over a range of calcination temperatures. The crystal configuration of the nanoparticles was inspected using XRD (Shimadzu model 6000, Shimadzu, Tokyo, Japan); the X-ray source, Cu Kα (0.154 nm), was utilised at room temperature in order to create diffraction patterns from the crystalline specimens within the 2θ range of 10–80°. TEM (model Hitachi H-7100 TEM, Hitachi, Tokyo, Japan) enabled visualisation of the shape, dimensions, and dimension distribution within the nanoparticle population; the accelerating voltage employed was 500 kV. The sample was procured by placing a dried aliquot of NiSe nanoparticle powder dispersed in deionised water onto copper grids. Finally, ESR spectroscopy (JEOL-JES-FA200, JEOL, Japan) was utilised to identify the magnetic properties of the nanoparticles at room temperature.

3. Results and discussion

3.1. *Thermal analysis*

Thermogravimetric analysis (TGA) was used for the thermal analysis of the metallic nitrate; a differential gravimetric technique (DTG) was employed for the thermal analysis of the PVP [44]. This facilitated the recognition of the superior temperature during calcination. The TG-DTA curves for the produced material that contained PVP (MW = 29,000 g/ml) metallic nitrate prior to calcination are illustrated in Fig. 1. After calcination, two separate weight reductions were depicted by the TGA curve. Initially, a weight attrition of approximately 16% was documented between the temperatures of 70 °C and 290 °C; this was attributed to water evaporation. The second weight decrease of approximately 84%, was recorded between the temperatures of 290 °C and 462 °C; this was ascribed to the breakdown of inorganic and organic substances from the nitrate salts and PVP, which gave rise to the generation of the stable NiSe material. A three-phase weight decrease was evidenced by the DTG curve. The first

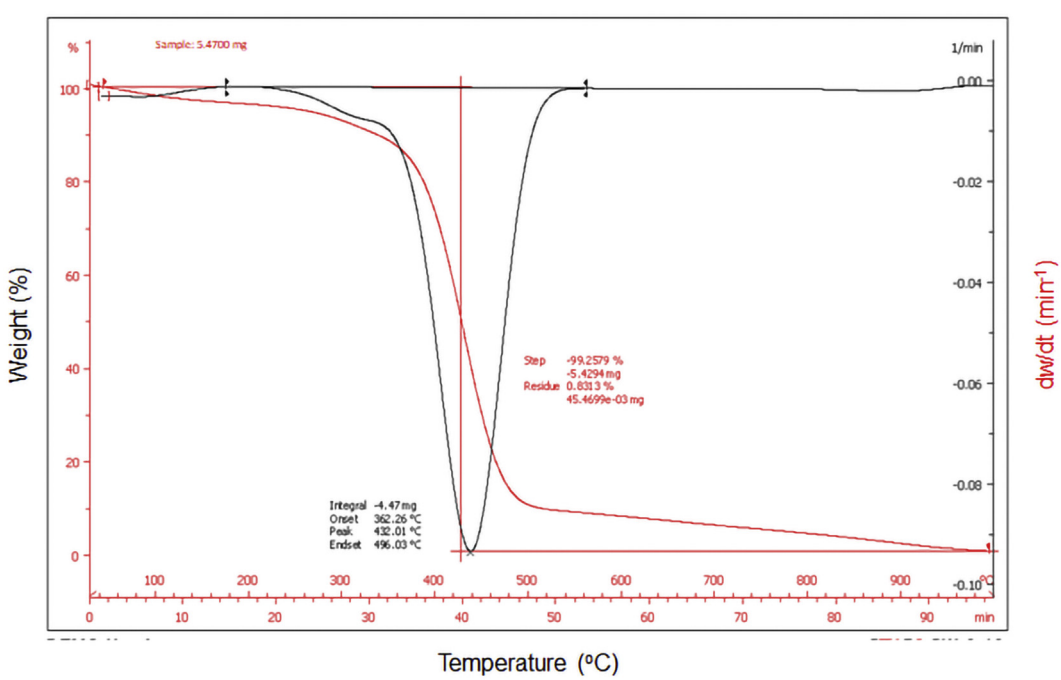

Fig. 1 – Heat rate of 10 °C/min was used to generate thermogravimetric (TG) and thermogravimetric derivative (DTG) curves for PVP/Nise.

phase was typical of moisture being caught within the sample and occurred at temperatures under 110 °C. A modest peak appeared at 362 °C, which was ascribed to the degradation of NOx compounds. Most of the PVP content of the sample degraded during the third phase, at 432 °C, the temperature of the greatest weight reduction. Minimal weight attrition was noted at 496 °C, potentially owing to the full conversion of the residual PVP into carbonaceous substances. At temperatures above 496 °C, no additional weight reduction was seen as any carbonaceous material had been eradicated from the sample between the temperatures of 432 °C and 496 °C. Following TGA, the black colouration altered to a crystalline pale grey, which implied the generation of NiSe nanoparticles containing minimal impurities.

3.2. *The formation of NiSe nanoparticles*

A schematic depicting the pathway of NiSe nanoparticle generation by the thermal treatment technique is shown in Fig. 2. There is a vigorous engagement between the capping agent, PVP and the ions (NiSe) via ionic bonding between the Ni ions and the amide part, through the PVP chain's oxygen. The PVP's amide residue gave rise to steric and electrostatic stability within the Ni and Se. Ni^+, Se^- and NO_3^- ions and the PVP amide group are present within the aqueous solution. Prior to the drying stage, the Ni^+ ions could begin to accept electrons that were free within the solution to generate an Ni metal atom, i.e., the nucleation process. During the drying period, at a temperature > 80 °C (Fig. 1), water evaporation commenced and PVP degradation began, thus decreasing the length of the polymer chains capping the Ni and Se atoms, and Ni^+ ions. The CO, CO_2, H_2 and NO_2 were formed during the calcination at temperatures between 500 °C and 800 °C when PVP was exposed to oxygen. The NiSe particles commenced their evolution when more diminutive NiSe nanoparticles clustered to form particles of increased dimensions once the PVP was eliminated. Simultaneously, after the oxygen-enriched calcination, Ni–O nanoparticles were able to become established. Subsequently, nitrogen gas was utilised during calcination in order to remove oxygen from potential Ni–O nanoparticles, thus facilitating the production of pure NiSe NPs [45].

3.2.1. *UV–Vis study*

Analysis of the effect of the spectrum of calcination temperatures on the NiSe nanoparticles was performed using UV-Vis. Fig. 3 illustrates the diffuse reflectance spectral data of the individual samples, which were examined between 200 and 800 nm at ambient temperature. During the generation of the ionic compound, NiSe (Ni^{2+} Se^{2-}), the outer electrons are made complete, i.e. from $4p^4$ to $4p^6$ electrons, by the receipt of Ni's $4s^2$ electrons. During the configuration of ionic solid NiSe semiconductor nanoparticles, the semiconductor characteristic of the nanomaterials stems from electron translocation between the valence band, i.e. $5s^2$ of Ni or $4p^6$ of Se, and the vacant conduction band [46].

Within the specimens, a single band was shown within the visualised regions, with peaks located at 385 nm and 439 nm, attributed to the existence of Ni^{2+} species. The increase in this outlier implies augmented particle dimensions for surface

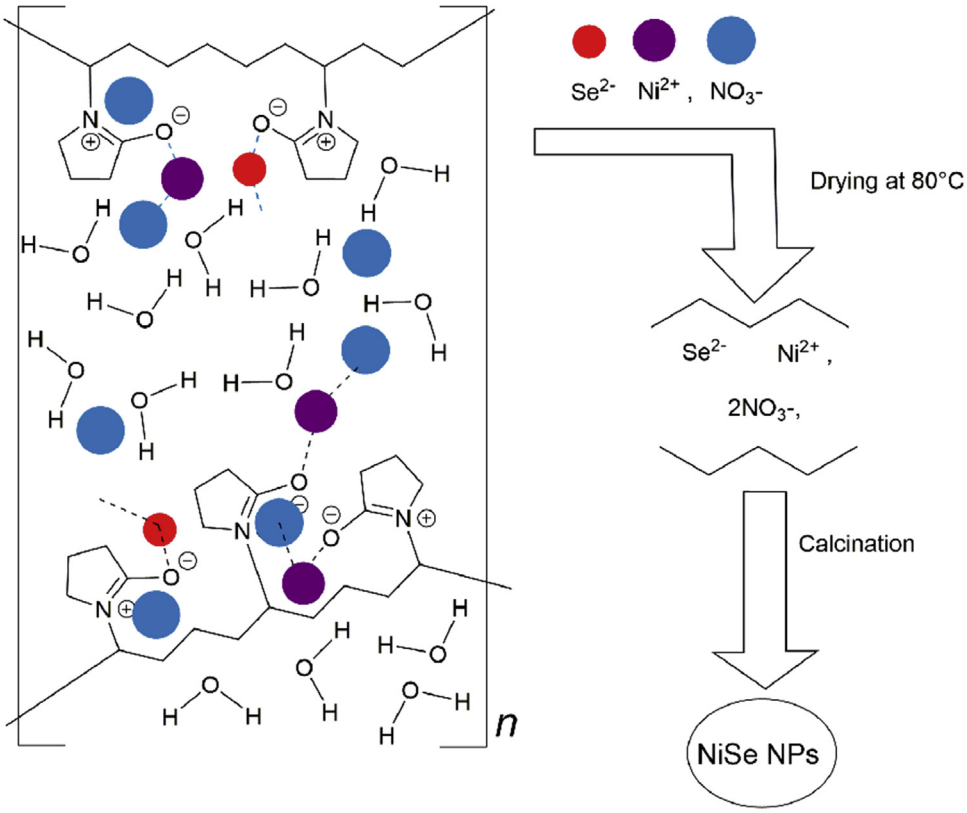

Fig. 2 – NiSe nanoparticles formed through the interactions between PVP, Se and Ni ions.

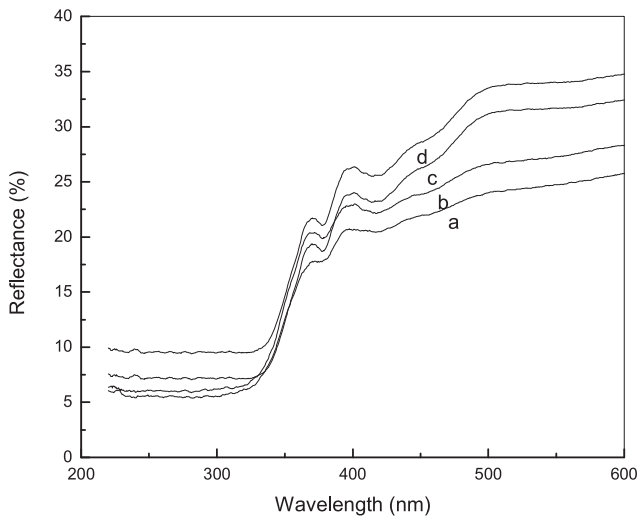

Fig. 3 – The diffuse reflectance spectra of NiSe nanoparticles formed at various calcination temperatures (a) 400, (b) 500, (c) 600, (d) 700, and (e) 800 °C.

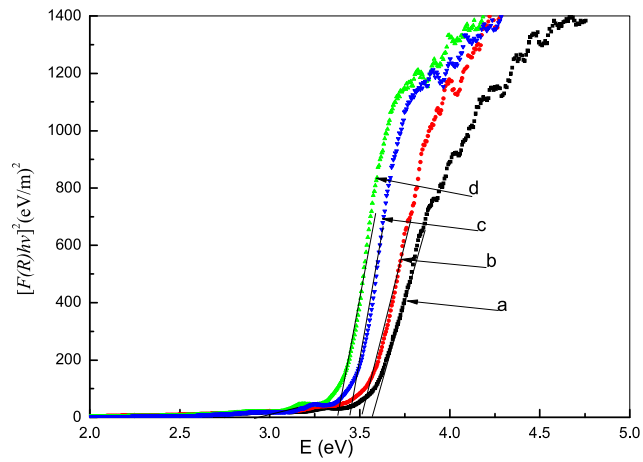

Fig. 4 – The band gaps of NiSe nanoparticles synthesized at the different calcination temperatures, (a) 500, (b) 600, (c) 700, and (d) 800.

NiSe nanoparticles following a rise in calcination temperatures.

The data from Fig. 3 were employed for computing the absorption coefficient, in accordance with the Kubelka-Munk (KM) formula [47,48]:

$$F(R^{\infty}) = \alpha/s = (1 - R^{\infty})/2R$$

where α and S indicate the absorption and scattering coefficients, respectively, and $F(R_{\infty})$ represents the KM function. The latter can be utilised in lieu of α in the diffused reflection spectra data in order to estimate the optical adsorption edge energy. A plot of $F(R_{\infty})E$ against E appeared linear close to the edge for direct allowed transition ($\eta = 1/2$). For each specimen, the point where the line crossed the abscissa ($F(R_{\infty})E = 0$) indicated the value of the optical absorption edge energy.

For the individual specimens undergoing calcination at varying temperatures, the optimal band gap data were computed utilising the reflectance spectra data and the KM formula [49]:

$$(F(R_{\infty}).\ h\upsilon)^2 = (A(h\upsilon\text{-}E_g))$$

where $F(R_{\infty})$ is the Kubelka-Munk function as before, $h\upsilon$ indicates the incident photon energy, A is a constant dependent on the probability of transition likelihood and diffuse reflectance, R_{∞}, and R_{∞} is the diffuse reflectance which is obtained from $R_{\infty} = R_{sample}/R_{standard}$.

A plot of $(F(R_{\infty}).\ h\upsilon)^2$ against $h\upsilon$ is depicted in Fig. 4. The linear spectra on the plot have been elongated towards the $h\upsilon$ axis in order to compute the ideal NiSe nanoparticle band gap values over a range of temperatures of calcination.

A fall in the optical band gap was noted in conjunction with increasing temperatures of calcination, i.e., from 3.54 eV to 3.37 eV at temperatures of 500 °C and 800 °C, respectively (Fig. 4). This decline in the energy band gap with elevating PVP can be attributed to the rise in particle dimension and rates of crystallinity, as demonstrated by the XRD results. It is believed that with enlarging particle dimensions, the number of atoms required for particle configuration becomes greater, which then enhances the valence and conduction elections within the particle ion centre [50]. The ultimate outcome is the reduction in particle band gap.

The energy band gap values of the generated NiSe nanoparticles were demonstrated to drop with an increase in calcination temperature (Fig. 4; Table 1). This change could be ascribed to the NiSe particle dimensions. It may also be explicated by alterations in the incompletely hidden valence and conduction bands of the Ni^{2+} ion d-shell electrons [51]. The effect of the particle dimensions on the band gap should be considered seriously. Owing to the rise in particle dimensions, the band configuration alters according to the substance properties. Increasing nanoparticle size narrows the band gap. Thus, at higher energy states, the s- and p-electron conduction bands are safeguarded but remotely, and at relatively big dimensions at a locus in greater proximity to the Fermi level, but which appears to be quite remote from the particle core. There is a notable nuclear potential of the conduction electrons; any modification encompassing allowed quantum numbers will evidence a rise in absorption energy, comparable to the energy of the conduction band.

3.3. *Phase composition analysis*

The analysis of systems containing multiple elements can be aided by FTIR spectroscopy, which generates results relating to the phase composition of the substance as well as the nature of the interactions between the various materials and

Table 1 – TEM, XRD and UV-Vis results of NiSe nanoparticles at calcination temperatures.

T °C	TEM nm	XRD nm	Eg eV
500	21 ± 4	19	3.58
600	33 ± 3	29	3.51
700	46 ± 5	41	3.44
800	54 ± 4	49	3.37

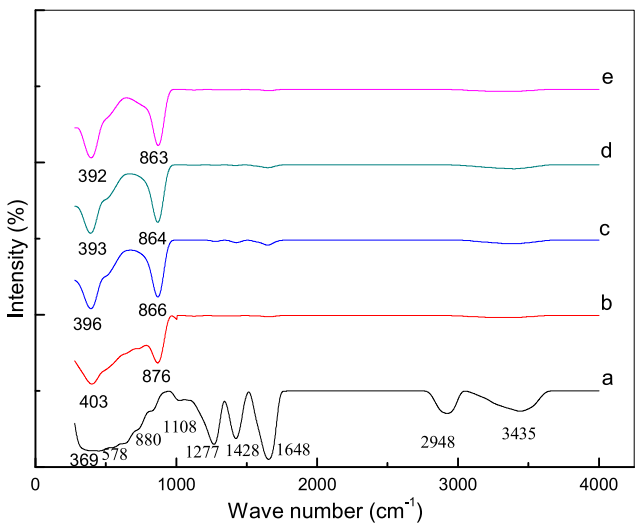

Fig. 5 – FTIR spectra of PVP and NiSe nanoparticles at: (a) ambient temperature, (b) 500 °C, (c) 600 °C, (d) 700 °C, and (e) 800 °C in the range of 280–4500 cm^{-1}.

polymers [52]. In the current work, FTIR was used to observe the extraction of PVP and to estimate the level of impurities within the NiSe nanoparticles generated throughout the range of calcination temperatures. The wavelength spectrum utilised was 280–4000 cm^{-1}; this demonstrated the organic and inorganic sample components at ambient temperature and following calcination at temperatures ranging between 500 °C and 800 °C.

The absorption peaks pertaining to PVP and the NiSe nanoparticles are demonstrated in Fig. 5. Prior to calcination, absorption peaks are seen at 3435 cm^{-1}, i.e. N–H vibration, 2948 cm^{-1}, i.e. C–H vibration and 1648 cm^{-1}, i.e. –C=C vibration covalent bond stretching (Fig. 5a). The absorption peaks observed at 1428 cm^{-1} indicate C–C in the ring, at 1277 cm^{-1}, C–N stretching, and at 1108 and 880 cm^{-1}, C–C in ring vibrations of covalent bonds. The C–O bond is indicated by absorption at 876 cm^{-1}. The vibration frequency of the Ni–Se ionic bond cohorts is seen at 369 cm^{-1} [53].

Fig. 5b depicts data from a sample that was calcined at 500 °C. Metallic bonds relating to Ni–Se could be generated under 403 cm^{-1} although peaks remain evident within the spectrum above 880 cm^{-1}. Peaks at $\leq$ 876 cm^{-1} pertain to the C–O bond vibrations, and arise from organic and PVP interactions, thus indicating only partial eradication of PVP from the sample at this particular calcination temperature.

The FTIR spectrum data from specimens obtained at calcination temperatures from 700 °C to 800 °C are illustrated in Fig. 5c, d and e. Two wide peaks are noted following calcination at 800 °C at 863 and 393 cm^{-1}, which correspond to C–O stretching vibrations and the symmetrical stretching bonds of Ni–Se, respectively; this pattern confirmed the presence of PVP in the sample as well as the organic incomplete C–O attachment. These findings imply that increasing the calcination temperature results in a higher degree of purity in the NiSe nanoparticles.

3.4. *Elemental composition analysis*

EDX spectroscopy was performed in order to identify the elemental constituents of the nanoparticle specimens generated by the thermal treatment approach. The results range for the NiSe nanoparticles through a calcination

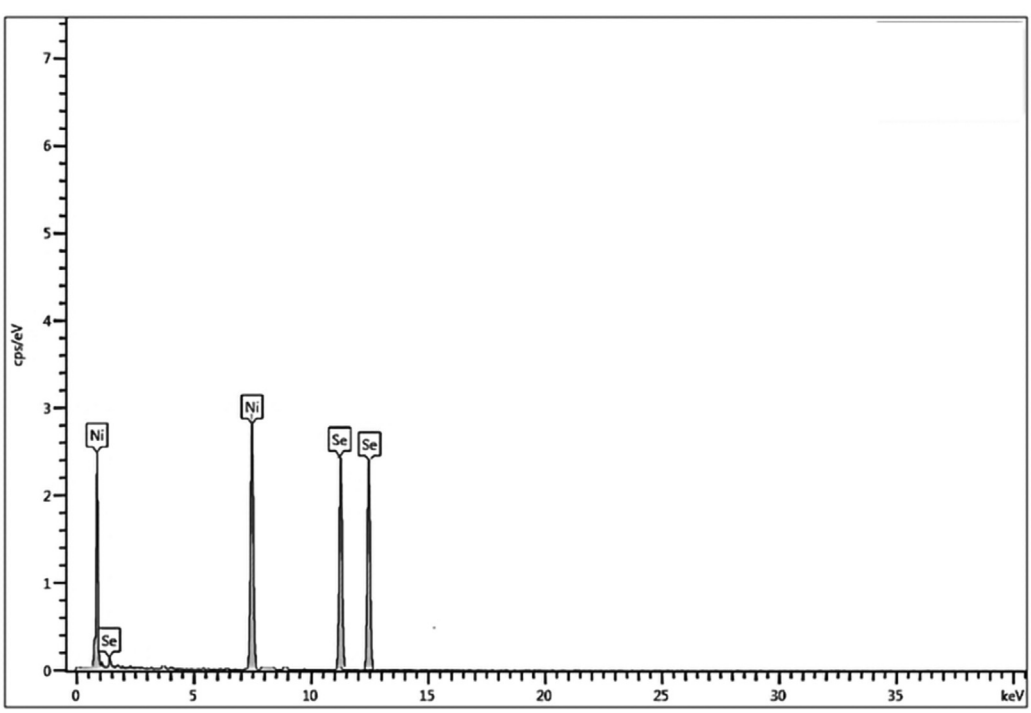

Fig. 6 – The EDX spectrum of the NiSe nanoparticles calcined at 700 °C.

temperature at 700 °C is depicted in Fig. 6. The relevant peaks indicate the NiSe elements within the sample. The documented NiSe anatomic proportions were 100.0%, indicative of the lack of impurities within the ultimate material. As a result, EDX results confirmed that pure NiSe nanoparticles were effectively produced by an utilised thermal treatment technique.

3.5. *Structural analysis*

Fig. 7 shows the structural properties of the samples examined with XRD before and after calcination. No diffraction peaks were observed on XRD in the sample at ambient temperature, i.e. prior to calcination, which only contained PVP and NiSe and was dried for 24 h at a temperature of 80 C. This indicates that the substance is amorphous, consisting of PVP, Ni, and Se ions; no crystalline composites have been observed prior to calcination.

In the samples that were calcined at temperatures ≥ 500 °C, configuration of crystalline NiSe nanoparticles was confirmed by the presence of diffraction peaks, with the following reflection planes present: (110), (101), (021), (102), (201), (103), (201), (202) and (104). At $2\theta = 32.5°$, a high-intensity peak corresponds to the crystal reflection plane with Miller indices of (110), which affirms the existence of NiSe nanoparticles with a hexagonal architecture in the specimens from the varying temperatures of calcination. These data are comparable with the standard phase documented in the XRD reference database, i.e. Reference code: 98-009-0267 for hexagonal NiSe crystals [54].

The XRD results show that increasing the calcination temperature causes higher and narrow diffraction peaks, indicating increased particle dimensions (Table 1). The crystallite dimensions within the specimens varied between 19 and 49 nm; these were computed utilising the Scherer formula from the full width at the half maximum (FWHM) peak widening of the maximum intensity peak (110) on the XRD plots [55–59]:

$$D(nm)=(k\lambda)/(\beta\cos\theta) \quad (1)$$

where D represents the dimension of the crystalline (nm); k reflects the shape factor, which for sphere particles equals 0.94; β refers to the FWHM measured in radians; λ is the X-ray

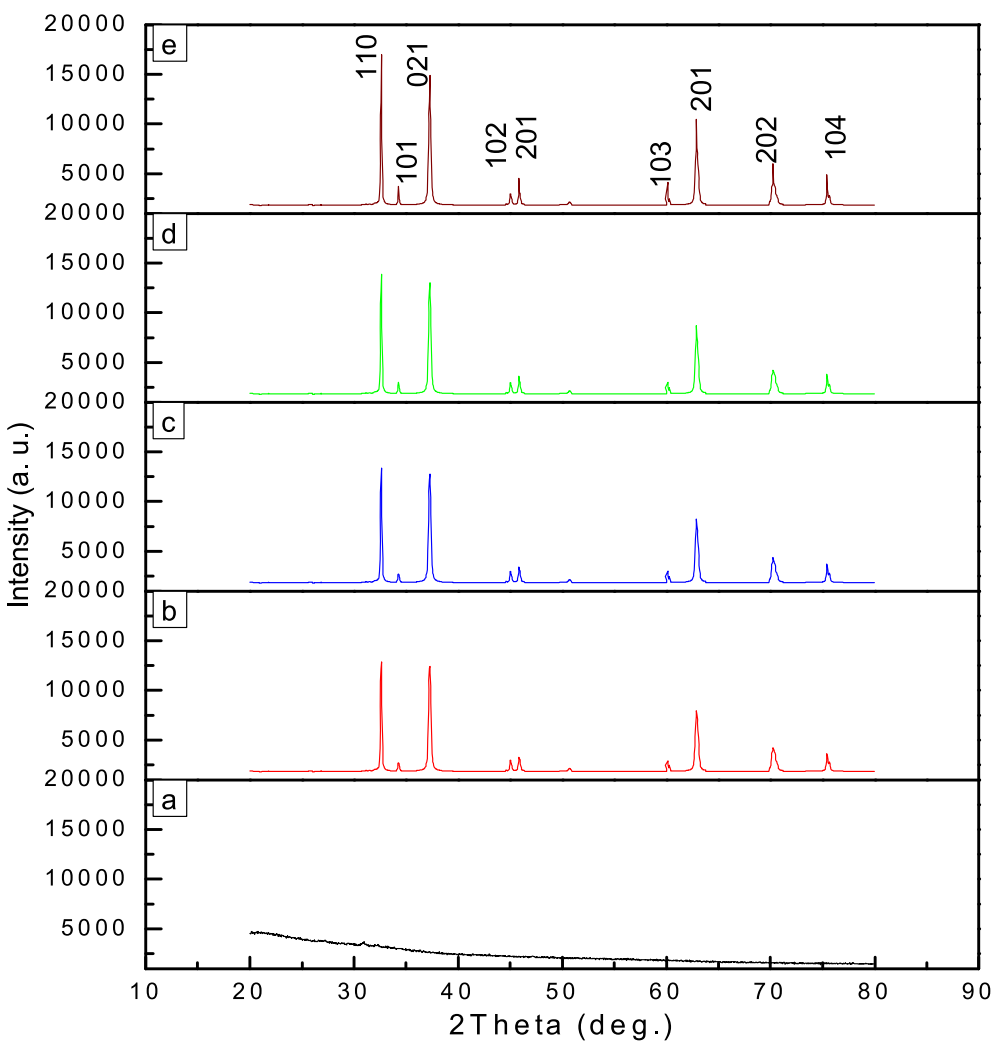

Fig. 7 – XRD patterns for NiSe nanoparticles calcined at: (a) ambient temperature, (b) 500 °C, (c) 600 °C, (d) 700 °C, and (e) 800 °C.

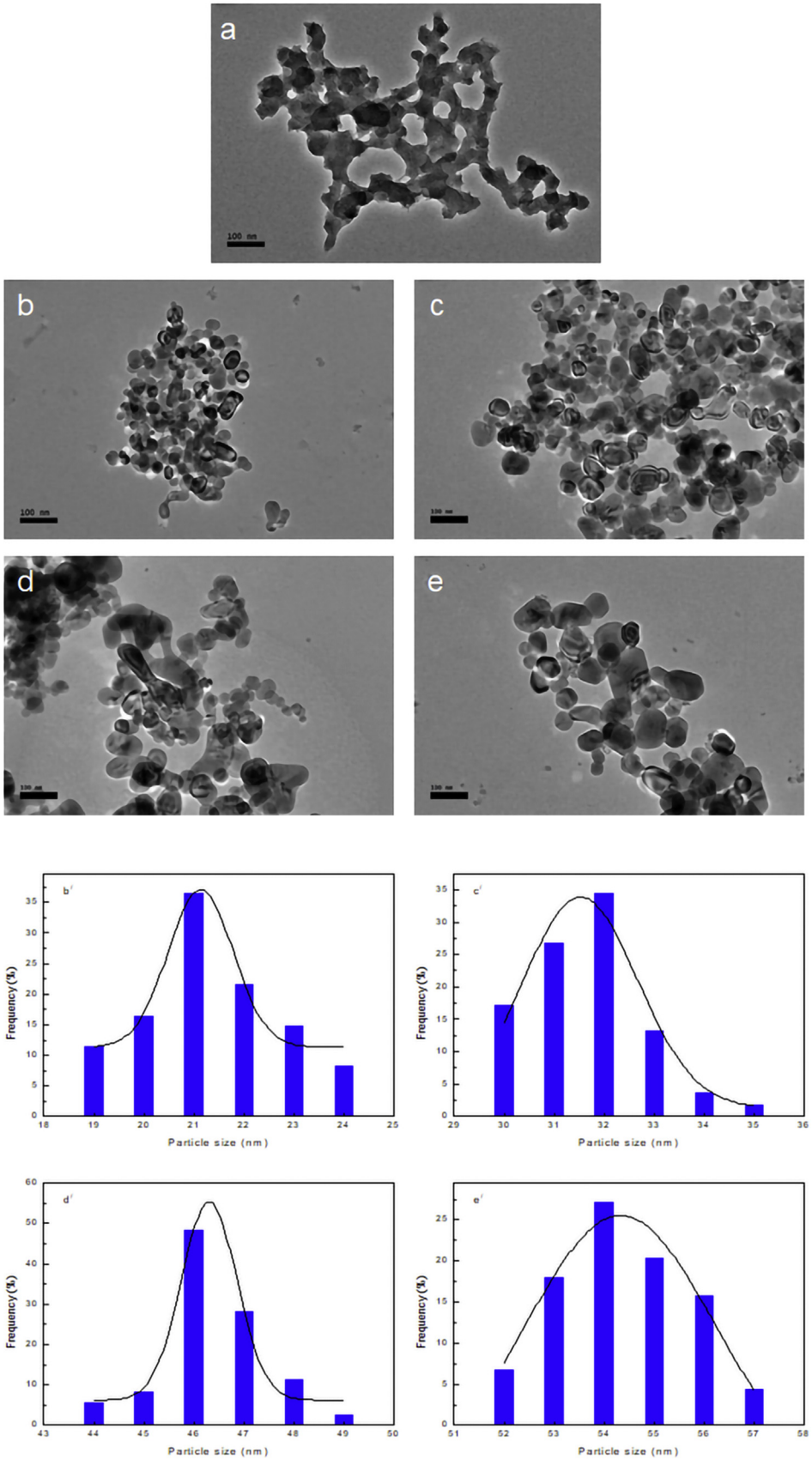

Fig. 8 – TEM image and particle size distribution of samples calcined at: (a) ambient temperature, (b, b′) 500 °C, (c, c′) 600 °C, (d, d′) 700 °C, and (e, e′) 800 °C.

wavelength of Cu Kα = 0.154 nm; and θ represents the Bragg angle.

3.6. TEM images analysis

The primary objective of the TEM was to examine the morphological and mean dimension distribution of the NiSe nanoparticles. The morphology of the NiSe nanoparticles was practically spherical, with homogeneity in shape and dimensional distribution for all the samples that underwent calcination at the various temperatures, as determined by TEM imaging. All of the TEM images are presented on a single scale of 100 nm (Fig. 8).

The mean particle dimensions for the respective calcination temperatures were: 21 nm, 500 °C; 33 nm, 600 °C; 46 nm, 700 °C; and 54 nm, 800 °C. These results were consistent with those obtained from XRD and confirm the increased particle size as the calcination temperature was raised [60–62].

Prior to calcination at a temperature of 500 °C, NiSe nanoparticle nucleation had already occurred. Application of heat during the thermal treatment triggered the liberation of electrons from medium substances and led to the generation of increased numbers of NiSe atoms. The heat additionally caused PVP degradation, leading to a gradual freeing of the capping property from the NiSe atoms and particles, respectively. The latter have a tendency to cluster to create NiSe nanoparticles of greater dimensions. The higher calcination temperatures caused the more weakly bonded PVP on the veneer of the particles to degrade as a result of the Oswald ripening pathway, thus facilitating clustering and the increased particle dimension. Conversely, the repulsive force generated by the conduction electrons that enclose the NiSe nanoparticles inhibited additional clustering. The rising calcination temperature caused an elevation in particle thermal vibration and kinesis, which also suppressed particle amassment. The clustering also leads to a rise in quantum dot particle size with rising calcination temperatures.

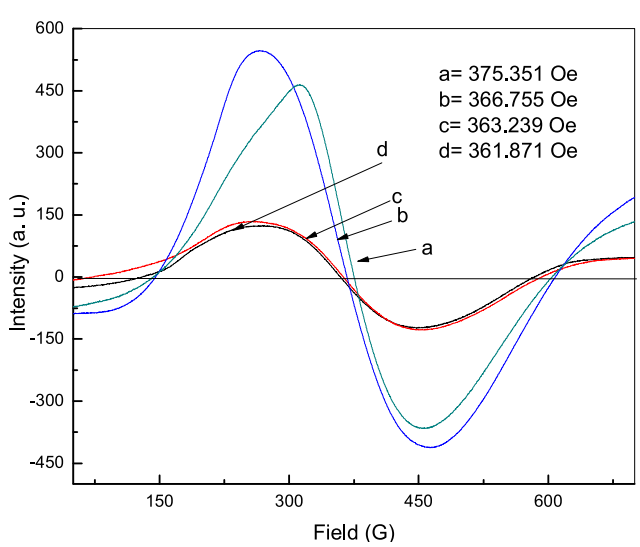

Fig. 9 – ESR spectra of NiSe nanoparticles at different calcination temperatures of, (a) 500 °C, (b) 600 °C, (c) 700 °C, and (de) 800 °C.

Table 2 – Magnetic parameters of NiSe nanoparticles observed for ESR analysis.

Calcination temperature (°C)	*g*- factor	*Hr* (Oe)
500	1.750194	375.351
600	1.791216	366.755
700	1.808554	363.239
800	1.815391	361.871

3.7. Electron spin resonance analysis

Fig. 9 illustrates the ESR spectrum data relating to the samples heated to calcination temperatures of 500 °C – 800 °C. There was a sequence of broadly ranging and frequently arising markers associated with the individual samples from the specific temperatures owing to the presence of the NiSe semiconductor nanoparticle unpaired conduction electrons. There are two potential sources of the ESR signal, i.e. a paramagnetic defect condition from inside the NiSe, or paramagnetic sample contamination. These findings infer those paramagnetic properties were present in the specimens.

A drop in resonant magnetic field intensity occurred with rising temperature, i.e. from 375.351 G at 500 °C to 361.871 G at 800 °C (Table 2). The *g*-factor parameters rose from 1.750194 to 1.815391 when the temperature was increased from 500 °C to 800 °C (Table 2). These results infer that the intrinsic magnetic field is enhanced owing to the increased calcination temperatures, thus implying that the microscopic magnetic exchanges are more frequent as the particle dimensions enlarge. The *g*-factor can be computed utilising the following formula [38]:

$$g = (h\upsilon)/(\beta \cdot Hr)$$

where *h, υ and* β indicate Planck's constant, the microwave frequency and the Bohr magneton (9.274×10^{-24} J T^{-1}), respectively; *Hr* represents the resonant magnetic field.

It can be assumed that the resonance magnetic field diminishes as the g-factor increases. Nevertheless, v is a constant in ESR spectroscopy. Elevated g-factor values and decreases in Hr, in keeping with the increased magnetisation values, have been noted in previous studies on NiSe nanoparticles.

4. Conclusion

NiSe nanoparticles were effectively manufactured using a straightforward thermal treatment approach, requiring only the components nickel nitrate, selenium, PVP and deionised water. Using oxygen and nitrogen gas flows during calcination facilitated the extraction of organic materials, leading to the synthesis of pure crystalline NiSe nanoparticles. A decline in conduction band energy was observed, from 3.54 eV to 3.37 eV at calcination temperatures of 500 °C and 800 °C, respectively; this was attributed to the increased particle dimensions generating higher attraction forces between the conduction electrons and metal ions. The benefits of this thermal treatment approach include its simplicity and the fact that it was pro-environmental, with no noxious or undesired by-products

requiring disposal. This indicates that the products can be applied to a broad variety of energy applications.

Author contributions

N.M.A.-H. conceived and designed the experiments; N.M.A.-H., R.M.K, A.M.A.-G., and M.A.S. performed the experiments; N.M.A.-H., A.M.A.-G., M.A.S., H.B., and A.M.N., analyzed the data; R.M.K., J.Y., J.L., S.X., B.A.A.-A. and A.M.N., contributed rea-gents/materials/analysis tools; N.M.A.-H., A.M.A.-G., and M.A.S. wrote the paper. All authors have read and agreed to the published version of the manuscript.

Declaration of Competing Interest

The authors declare that they have no known competing financial interests or personal relationships that could have appeared to influence the work reported in this paper.

Acknowledgments

This research was supported in part by the Research Foundation for Advanced Talents of Dezhou University, in part by Taishan Scholars Program of Shandong Province (tsqn201812104), the Qingchuang Science and Technology Plan of Shandong Province (2019KJJ017), in part by researchers supporting project number (RSP-2021/348) King Saud University, Riyadh, Saudi Arabia, and in part by Universiti Teknologi Malaysia (UTM), Fellow Research Grant, Q.J130000.21A6.00P19, in part by Tenaga Nasional Berhad (TNB) and Universiti Tenaga Nasional (UNITEN) with Grant Code: (J510050002/2021048). Also, this research is supported by the TNB SEED FUND with Grant Code: (U-TL-RD-21).

REFERENCES

[1] Theerthagiri J, Karuppasamy K, Durai G, Rana AUHS, Arunachalam P, Sangeetha K, et al. Recent advances in metal chalcogenides (MX; X= S, Se) nanostructures for electrochemical supercapacitor applications: a brief review. Nanomaterials 2018;8:256.
[2] Deng W, Chen J, Yang L, Liang X, Yin S, Deng X, et al. Solid solution metal chalcogenides for sodium-ion batteries: the recent advances as anodes. Small 2021;17:2101058.
[3] Bafekry A, Faraji M, Fadlallah M, Jappor H, Hieu N, Ghergherehchi M, et al. Prediction of two-dimensional bismuth-based chalcogenides Bi2X3 (X= S, Se, Te) monolayers with orthorhombic structure: a first-principles study. J Phys Appl Phys 2021;54:395103.
[4] Absi E, Saleh M, Al-Hada NM, Hamzah K, Alhawsawi AM, Banoqitah EM. A review on preparation and characterization of silver/nickel oxide nanostructures and their applications. Appl Phys A 2021;127:1–32.
[5] Al-Hada NM, Kamari HM, Abdullah CAC, Saion E, Shaari AH, Talib ZA, et al. Down-top nanofabrication of binary (CdO) x (ZnO) 1–x nanoparticles and their antibacterial activity. Int J Nanomed 2017;12:8309.
[6] Al-Mushki AA, Ahmed AAA, Abdulwahab A, Al-Asbahi BA, Abduljalil J, Saad FA, et al. Structural, optical, and antibacterial characteristics of mixed metal oxide CdO–NiO–Fe2O3 nanocomposites prepared using a self-combustion method at different polyvinyl alcohol concentrations. Appl Phys A 2022;128:1–15.
[7] Subbarao U, Marakatti VS, Amshumali MK, Loukya B, Singh DK, Datta R, et al. Size and morphology controlled NiSe nanoparticles as efficient catalyst for the reduction reactions. J Solid State Chem 2016;244:84–92.
[8] Jorgensen CK. Inorganic complexes. Elsevier; 2012.
[9] Mada R. Engineering of semiconductor nanocrystals and metal ions in amorphous materials. 2021.
[10] Umapathi S. Transition metal chalcogenide hybrid systems as catalysts for energy conversion and biosensing. Missouri University of Science and Technology; 2020.
[11] Pathak M, Tamang D, Kandasamy M, Chakraborty B, Rout CS. A comparative experimental and theoretical investigation on energy storage performance of CoSe2, NiSe2 and MnSe2 nanostructures. Appl Mater Today 2020;19:100568.
[12] Qaseem A, Chen F, Zhang N. Ag-Cu nanoalloys as oxygen reduction electrocatalysts in alkaline media for advanced energy conversion and storage. Adv Catal Mater: Photocatal Other Current Trends 2016;415.
[13] Zafar F. In-situ fabrication of metal organic frameworks nanocomposite for oxygen reduction reaction. 2021.
[14] Walter C, Menezes PW, Driess M. Perspective on intermetallics towards efficient electrocatalytic water-splitting. Chem Sci 2021;12:8603–31.
[15] Dorontić S, Jovanović S, Bonasera A. Shedding light on graphene quantum dots: key synthetic strategies, characterization tools, and cutting-edge applications. Materials 2021;14:6153.
[16] Wan K. Development of nickel and cobalt-based materials for the electrocatalytic oxygen evolution reaction. 2021.
[17] Lu H, Tournet J, Dastafkan K, Liu Y, Ng YH, Karuturi SK, et al. Noble-metal-free multicomponent nanointegration for sustainable energy conversion. Chem Rev 2021;121:10271–366.
[18] Woods-Robinson R, Han Y, Zhang H, Ablekim T, Khan I, Persson KA, et al. Wide band gap chalcogenide semiconductors. Chem Rev 2020;120:4007–55.
[19] Patrick TKH. Design and fabrication of III-V semiconductor nanostructures by molecular beam epitaxy. 2014.
[20] Reshetilov A, Iliasov P, Reshetilova T, Rai M. Nanobiosensors and their applications. In: Metal nanoparticles in microbiology. Springer; 2011. p. 269–83.
[21] Ghobadi N, Akbari Badakhshan T. Shapes alteration and optical band gap controlling in NiSe nanostructure thin films with deposition temperature changing. Optik 2015;126:4557–60. https://doi.org/10.1016/j.ijleo.2015.08.052.
[22] Yang J, Sun Z, Wang J, Zhang J, Qin Y, You J, et al. Hierarchical NiSe 2 spheres composed of tiny nanoparticles for high performance asymmetric supercapacitors. CrystEngComm 2019;21:994–1000.
[23] Li X, Han G-Q, Liu Y-R, Dong B, Hu W-H, Shang X, et al. NiSe@NiOOH core–shell hyacinth-like nanostructures on nickel foam synthesized by in situ electrochemical oxidation as an efficient electrocatalyst for the oxygen evolution reaction. ACS Appl Mater Interfaces 2016;8:20057–66.
[24] Li Y, Yan D, Zou Y, Xie C, Wang Y, Zhang Y, et al. Rapidly engineering the electronic properties and morphological structure of NiSe nanowires for the oxygen evolution reaction. J Mater Chem 2017;5:25494–500.
[25] Zhang X, Zhen M, Bai J, Jin S, Liu L. Efficient NiSe-Ni3Se2/graphene electrocatalyst in dye-sensitized solar cells: the role of hollow hybrid nanostructure. ACS Appl Mater Interfaces 2016;8:17187–93.

[26] Bhat KS, Nagaraja H. Nickel selenide nanostructures as an electrocatalyst for hydrogen evolution reaction. Int J Hydrogen Energy 2018;43:19851–63.
[27] Meng L, Wu Y, Zhang T, Tang H, Tian Y, Yuan Y, et al. Highly conductive NiSe 2 nanostructures for all-solid-state battery–supercapacitor hybrid devices. J Mater Sci 2019;54:571–81.
[28] Esmailzadeh S, Shahrabi T, Darband GB, Yaghoubinezhad Y. Pulse electrodeposition of nickel selenide nanostructure as a binder-free and high-efficient catalyst for both electrocatalytic hydrogen and oxygen evolution reactions in alkaline solution. Electrochim Acta 2020;334:135549.
[29] Lee Y-H, Kang JS, Jo I-R, Sung Y-E, Ahn K-S. Double-layer cobalt selenide/nickel selenide with web-like nanostructures as a high-performance electrode material for supercapacitors. J Electroanal Chem 2021:115479.
[30] Zhao J, Yang L, Li H, Huang T, Cheng H, Meng A, et al. Ni3Se2 nanosheets in-situ grown on 3D NiSe nanowire arrays with enhanced electrochemical performances for supercapacitor and efficient oxygen evolution. Mater Char 2021;172:110819. https://doi.org/10.1016/j.matchar.2020.110819.
[31] He L, Wang Y, Guo Y, Li G, Zhang X, Cai W. Core– shell NiSe/Ni (OH) 2 with NiSe nanorods and Ni (OH) 2 nanosheets as battery-type electrode for hybrid supercapacitors. Nanotechnology 2021;32:345706.
[32] Tian Y, Ruan Y, Zhang J, Yang Z, Jiang J, Wang C. Controllable growth of NiSe nanorod arrays via one-pot hydrothermal method for high areal-capacitance supercapacitors. Electrochim Acta 2017;250:327–34.
[33] Zhai L, Mak CH, Qian J, Lin S, Lau SP. Self-reconstruction mechanism in NiSe2 nanoparticles/carbon fiber paper bifunctional electrocatalysts for water splitting. Electrochim Acta 2019;305:37–46.
[34] Khan M, Khan A, Khan H, Ali N, Sartaj S, Malik S, et al. Development and characterization of regenerable chitosan-coated nickel selenide nano-photocatalytic system for decontamination of toxic azo dyes. Int J Biol Macromol 2021;182:866–78.
[35] Esmailzadeh S, Shahrabi T, Yaghoubinezhad Y, Darband GB. Optimization and characterization of pulse electrodeposited nickel selenide nanostructure as a bifunctional electrocatalyst by response surface methodology. Int J Hydrogen Energy 2021;46:18898–912.
[36] Salem A, Saion E, Al-Hada NM, Kamari HM, Shaari AH, Abdullah CAC, et al. Synthesis and characterization of CdSe nanoparticles via thermal treatment technique. Results Phys 2017;7:1556–62.
[37] Salem A, Saion E, Al-Hada NM, Kamari HM, Shaari AH, Radiman S. Simple synthesis of ZnSe nanoparticles by thermal treatment and their characterization. Results Phys 2017;7:1175–80.
[38] Gene SA, Saion E, Shaari AH, Kamarudin MA, Al-Hada NM, Kharazmi A. Structural, optical, and magnetic characterization of spinel zinc chromite nanocrystallines synthesised by thermal treatment method. J Nanomater 2014;2014.
[39] Al-Hada NM, Saion E, Talib ZA, Shaari AH. The impact of polyvinylpyrrolidone on properties of cadmium oxide semiconductor nanoparticles manufactured by heat treatment technique. Polymers 2016;8:113.
[40] Al-Hada NM, Al-Ghaili AM, Kasim H, Saleh MA, Baqiah H, Liu J, et al. Nanofabrication of (Cr2O3) x (NiO) 1-x and the impact of precursor concentrations on nanoparticles conduct. J Mater Res Technol 2021;11:252–63.
[41] Al-Hada NM, Al-Ghaili AM, Kasim H, Saleh MA, Flaifel MH, Kamari HM, et al. The effect of PVP concentration on particle size, morphological and optical properties of cassiterite nanoparticles. IEEE Access 2020;8:93444–54.
[42] Alzahrani JS, Midala IH, Kamari HM, Al-Hada NM, Tim CK, Nidzam NNS, et al. Effect of calcination temperature on the structural and optical properties of (ZnO) 0.8 (ZrO2) 0.2 nanoparticles. J Inorg Organomet Polym Mater 2022:1–11.
[43] Absi E, Saleh MA, Al-Hada NM, Hamzah K, Alhawsawi AM, Banoqitah EM. Binary nickel and silver oxides by thermal route: preparation and characterization. Appl Phys A 2021;127:1–11.
[44] Baqer AA, Matori KA, Al-Hada NM, Shaari AH, Kamari HM, Saion E, et al. Synthesis and characterization of binary (CuO) 0.6 (CeO2) 0.4 nanoparticles via a simple heat treatment method. Results Phys 2018;9:471–8.
[45] Gharibshahi L, Saion E, Gharibshahi E, Shaari AH, Matori KA. Structural and optical properties of Ag nanoparticles synthesized by thermal treatment method. Materials 2017;10:402.
[46] Moloto N, Moloto MJ, Coville NJ, Sinha Ray S. Optical and structural characterization of nickel selenide nanoparticles synthesized by simple methods. J Cryst Growth 2009;311:3924–32. https://doi.org/10.1016/j.jcrysgro.2009.06.006.
[47] Kothandan D, Jeevan Kumar R, Chandra Babu Naidu K. Barium titanate microspheres by low temperature hydrothermal method: studies on structural, morphological, and optical properties. J Asian Ceram Soc 2018;6:1–6.
[48] Mallikarjuna A, Ramesh S, Kumar NS, Naidu KCB, Ratnam KV, Manjunatha H, et al. Structural transformation and high negative dielectric constant behavior in (1-x)(Al0· 2La0· 8TiO3)+(x)(BiFeO3)(x= 0.2–0.8) nanocomposites. Phys E Low-dimens Syst Nanostruct 2020;122:114204.
[49] Al-Hada NM, Saion EB, Shaari AH, Kamarudin MA, Flaifel MH, Ahmad SH, et al. A facile thermal-treatment route to synthesize ZnO nanosheets and effect of calcination temperature. PLoS One 2014;9:e103134.
[50] Al-Hada NM, Saion E, Kamari HM, Flaifel MH, Shaari AH, Talib ZA, et al. Structural, morphological and optical behaviour of PVP capped binary (ZnO) 0.4 (CdO) 0.6 nanoparticles synthesised by a facile thermal route. Mater Sci Semicond Process 2016;53:56–65.
[51] Moloto N, Moloto M, Coville N, Ray SS. Optical and structural characterization of nickel selenide nanoparticles synthesized by simple methods. J Cryst Growth 2009;311:3924–32.
[52] Naresh U, Kumar RJ, Naidu KCB. Hydrothermal synthesis of barium copper ferrite nanoparticles: nanofiber formation, optical, and magnetic properties. Mater Chem Phys 2019;236:121807.
[53] Al-Hada NM, Saion EB, Shaari AH, Kamarudin MA, Flaifel MH, Ahmad SH, et al. A facile thermal-treatment route to synthesize the semiconductor CdO nanoparticles and effect of calcination. Mater Sci Semicond Process 2014;26:460–6. https://doi.org/10.1016/j.mssp.2014.05.032.
[54] Sobhani A, Salavati-Niasari M. Synthesis and characterization of a nickel selenide series via a hydrothermal process. Superlattice Microst 2014;65:79–90.
[55] Kumar NS, Suvarna RP, Naidu KCB. Multiferroic nature of microwave-processed and sol-gel synthesized NanoPb1-xCoxTiO3 (x= 0.2–0.8) ceramics. Cryst Res Technol 2018;53:1800139.
[56] Kumar DS, Naidu KCB, Rafi MM, Nazeer KP, Begam AA, Kumar GR. Structural and dielectric properties of superparamagnetic iron oxide nanoparticles (SPIONs) stabilized by sugar solutions. Mater Sci Pol 2018;36:123–33.
[57] Raghuram N, Rao TS, Naidu KCB. Electrical and impedance spectroscopy properties of hydrothermally synthesized Ba0.

2Sr0. 8-yLayFe12O19 (y= 0.2–0.8) nanorods. Ceram Int 2020;46:5894–906.

[58] Al-Hada NM, Md. Kasmani R, Kasim H, Al-Ghaili AM, Saleh MA, Banoqitah EM, et al. The effect of precursor concentration on the particle size, crystal size, and optical energy gap of CexSn1–xO2 nanofabrication. Nanomaterials 2021;11:2143.

[59] Al-Hada NM, Kamari HM, Saleh MA, Flaifel MH, Al-Ghaili AM, Kasim H, et al. Morphological, structural and optical behaviour of PVA capped binary (NiO) 0.5 (Cr2O3) 0.5 nanoparticles produced via single step based thermal technique. Results Phys 2020;17:103059.

[60] Al-Hada NM, Kamari HM, Shaari AH, Saion E. Fabrication and characterization of Manganese–Zinc Ferrite nanoparticles produced utilizing heat treatment technique. Results Phys 2019;12:1821–5.

[61] Mallikarjuna A, Kumar NS, Babu TA, Ramesh S, Naidu K. Structural and Dielectric Properties of (1-x)(Al0. 2La0. 8TiO3)+(x)(BiZnFeO3)(x= 0.2– 0.8) nanocomposites. J Inorg Organomet Polym Mater 2021;31:4512–22.

[62] Naidu KCB, Wuppulluri M. Ceramic nanoparticle synthesis at lower temperatures for LTCC and MMIC technologies. IEEE Trans Magn 2018;54:1–8.